

Vision Based Autonomous UAV Plane Estimation And Following for Building Inspection

Yang Lyu, *Member, IEEE*, Muqing Cao, Shenghai Yuan, and Lihua Xie, *Fellow, IEEE*

Abstract—Unmanned Aerial Vehicle (UAV) has already demonstrated its potential in many civilian applications, and the façade inspection is among the most promising ones. In this paper, we focus on enabling the autonomous perception and control of a small UAV for a façade inspection task. Specifically, we consider the perception as a planar object pose estimation problem by simplifying the building structure as concatenation of planes, and the control as an optimal reference tracking control problem. First, a vision based adaptive observer is proposed which can realize stable plane pose estimation under very mild observation conditions. Second, a model predictive controller is designed to achieve stable tracking and smooth transition in a multiple planes scenario, while the persistent excitation (PE) condition of the observer and the maneuver constraints of the UAV are satisfied. The proposed autonomous plane pose estimation and plane tracking methods are tested in both simulation and practical building façade inspection scenarios, which demonstrate their effectiveness and practicability.

I. INTRODUCTION

Autonomous vehicle, especially the Unmanned Aerial Vehicle (UAV) has attracted tremendous research interests in recent years due to its potential capability of improving efficiency and safety in many military and civilian applications [1]. Among them, the building *façade inspection* is considered as one of the most promising applications for small size UAVs [2]. During a façade inspection task, a UAV has to maintain a desired distance to the building façades while following an inspection path allows its on-board inspection sensors to cover the entire surface area of the building. To carry out the challenging autonomous inspection task, the UAV needs to persistently measure the unknown building structure and continuously control the vehicle so as to effectively cover the building façades. In this paper, we focus on solving the façade plane pose estimation and optimal plane following control together, thus demonstrating autonomous and efficient façade inspection capability.

The estimation of the façade pose is a prerequisite for autonomous inspection of a subject whose detailed structural information is unknown. The inspection subject, e.g., a building, often has significant structural features, such as points, lines and planes. With proper clustering techniques [3], [4], most buildings can be approximated as multiple concatenated planes, therefore makes the plane one of the most ubiquitous geometric primitives in an inspection scenario. There are multiple sensing options for the plane estimation,

such as camera [5], RGB-D camera [6], LiDAR [7], and sonar sensor [8]. The LiDAR sensor is often considered with unparalleled sensing capabilities for robot 3-D space operations. Nevertheless, its high payload requirement may hinder its practical implementation on small UAV with limited payload capabilities. On the other hand, the camera, with its low payload requirement and high fidelity sensing information, is considered as the most common sensor for robot operation. By taking 2D image information from multiple views, the 3D geometry of object can be retrieved [9], [10]. Therefore, besides serving as an inspection sensor of the building façade, we consider to implement the camera on-board a moving platform to estimate the pose of the planar façades.

The research on vision based structure estimation has been active for years. Methods may be roughly divided into two streams, namely the homography based methods [5], [11], and direct depth estimation methods [12]–[15]. The first method exploits the homography constraint to recover the spatial structure from a moving camera observing feature points. The homography matrix is calculated from feature correspondences of 2D image pairs. As illustrated in [11], an extended Kalman filter is implemented to estimate the landing plane, with vision measurements derived from the homography relationship. A more recent result reported in [5] utilizes a 2D homography matrix to recover the plane scale information from the ground plane and camera with constant height. As the homography based method depends on the feature correspondences, which may require further treatment of features variation and therefore hinder its robustness in a dynamic scenario. The second method [12]–[16] is to obtain the structural information, such as the depth map, based on the structure from motion (SfM) [17]. Among them, the active vision scheme proposed in [12] is a well established method for depth estimation in 3-D scenarios. Subsequent works [13] and [14] extended the proposed framework to more structural scenarios, such as plane, sphere, and cylinder. The framework was proved to be locally exponentially stable under the persistent excitation condition that the sensor has a non-zero velocity. However it may still suffer from coupling and nonlinearity. To overcome those drawbacks, [15] proposed an improvement by decoupling the model into a linear form. In general the second method is more applicable than the first method during a mobile robot operation as it applies frame by frame feature tracking and is robust to feature gain/loss. More recently, the learning based method becomes a new trend by training a deep neural network to infer depth from images [18]–[20]. Nevertheless, the learning based method may still not be ready for field applications due to its high dependency

Yang Lyu, Muqing Cao, Shenghai Yuan and Lihua Xie (corresponding author) are with School of Electrical and Electronic Engineering, Nanyang Technological University, 50 Nanyang Avenue, Singapore 639798. (email: {lyu.yang, mqcao, shyuan, elhxie}@ntu.edu.sg)

on training data and high computation cost. Therefore in this paper we consider implementing an observer based on SfM to realize stable plane pose estimation during an inspection task.

After measuring the plane pose, the plane path following for the inspection needs to be designed accordingly. With known inspection subject information, the path design is nothing more than the most commonly researched coverage path planing [8], [21], [22]. A detailed review of the coverage path planing with a known inspection map is given in [21], where different modeling patterns of coverage path planing are detailed. For instance, [8] proposed a space sampling based method for probabilistic complete path planing, where the availability of a 3-D CAD model is assumed. [22] described a coverage path planing method by dividing the known target region into several regular triangulations and then designing a path satisfying different constraints, such as sensing range, map coverage, collision avoidance. A more realistic assumption is that, although a global map is available, the inspection platform still needs to properly adjust its trajectory based on the measurement from the on-board sensors due to unforeseen situations, such as map inaccuracy, obstacle avoidance, etc. An on-line path re-planing algorithm for underwater structural inspection using autonomous robot is proposed in [8]. With a given initial nominal path based on a priori information, the re-planing is to continuously adjust the nominal path based on stochastic trajectory optimization and measurements from an on-board sonar sensor. Similar frameworks are also presented in [23], [24].

In the more challenging scenario without an accurate structure map, the vehicle is controlled based on local observation feedbacks to properly follow the façades of an inspection subject. The path following control of a UAV w.r.t. to planar surfaces is studied in [25], where the planar surfaces are detected based on cameras and a PID controller is designed with optical flow measurement feedbacks. Further, a receding horizon control law is proposed in [26] that enables a fixed wing UAV to follow the ground plane, with a given lateral trajectory. More recently, a nonlinear Model Predictive Control (MPC) method is implemented in [27] to solve the terrain following problem for an underwater vehicle during a seabed survey task. Inspired by the works aforementioned, we aim at designing an on-line path planing method based on the MPC framework, which is known for its optimality and constraints satisfaction, to realize the plane following while comply with the façade inspection requirement.

In this paper, we focus on solving the autonomous façade inspection with regard to an unknown inspection subject. On-line solutions for both vision based façade plane pose estimation and optimal inspection control are provided. First, the building façades are approximately modeled as concatenation of planes and a vision based plane pose observer is proposed. Upon that, a constrained MPC based plane following control strategy which incorporates inspection preferences is designed. The contributions of the paper are two folds. First, we propose a vision based observer to directly estimate the normal vector and depth of a plane from 2D image features of consecutive frames. The PE condition that guarantee the asymptotic stability is investigated. Second, we design a MPC based plane fol-

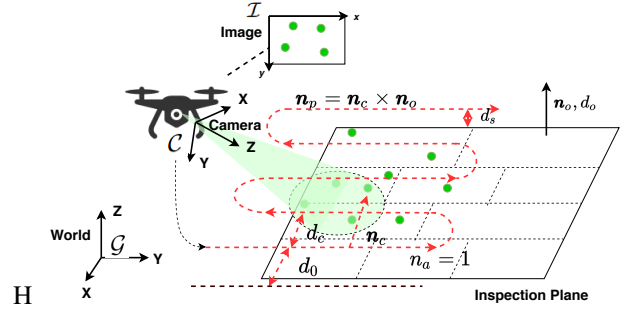


Figure 1. The coordination system illustration and inspection preferences.

lowing controller that bears multiple constraints, including PE condition and state and control constraints. The feasibility and stability are guaranteed by designing an appropriate adaptive reference update law and terminal conditions. The proposed framework is validated in practical inspection scenarios.

The remaining of the paper is organized as follows: Section II models the inspection problem as plane estimation and path following problems for UAV, and Section III and Section IV respectively describe the plane pose estimation and plane following control. Section V and Section VI describe the simulation and experimental results based on the proposed methods respectively. Section VII concludes the paper.

II. PROBLEM FORMULATION

The façade inspection problem using a UAV platform is formulated in this section. Specifically, the inspection task is to simultaneously estimate and follow a planar object based on an on-board vision sensor.

The process of the building inspection task and the coordinates are illustrated in Fig.1. First, the plane pose parameters are estimated in the camera frame, denoted as \mathcal{C} , based on the 2D measurements from the image frame, denoted as \mathcal{I} . Then the plane parameters are transformed to the global frame, denoted as \mathcal{G} , where the inspection preferences are described and the plane following controller is executed.

A. Models

1) *Planar object*: Let $\mathcal{O} = \{\mathbf{n}_o, d_o\}$ denote a plane. A point \mathbf{p} that belongs to \mathcal{O} satisfies

$$\mathbf{n}_o^T \mathbf{p} + d_o = 0,$$

where $\mathbf{n}_o = [n_x, n_y, n_z]^T \in \mathbb{S}^2$ is the plane unit normal vector and $d_o \in \mathbb{R}$ is the distance of \mathcal{O} to the original point of a specific coordinate system. Further in the homogeneous coordinate, the above equation can be written as $\bar{\mathbf{n}}_o \bar{\mathbf{p}} = 0$, where $\bar{\mathbf{p}} = [\mathbf{p}^T, 1]^T$, $\bar{\mathbf{n}}_o = [\mathbf{n}_o^T, d_o]^T$. The $\bar{\mathbf{n}}_o$ is not known a priori and needs to be estimated during the inspection operation.

2) *Moving platform*: For simplification, the platform is modeled as a discrete-time second order dynamics system in 3-D space:

$$\mathbf{x}_{k+1} = \mathbf{A}\mathbf{x}_k + \mathbf{B}\mathbf{u}_k, \quad (1)$$

where

$$\mathbf{A} = \begin{bmatrix} 1 & T_s \\ 0 & 1 \end{bmatrix} \otimes \mathbf{I}_3, \mathbf{B} = \begin{bmatrix} 0.5T_s^2 \\ T_s \end{bmatrix} \otimes \mathbf{I}_3,$$

and the state vector $\mathbf{x}_k = [\mathbf{p}_k^T, \mathbf{v}_k^T]^T \in \mathbb{R}^6$ includes the position and velocity of the platform at time instance $k \in \mathbb{Z}^+$ in the global frame \mathcal{G} . T_s is the sampling time interval between time instance. \mathbf{u}_k is the acceleration control input. Norm constraints are imposed on the velocity and acceleration control, as

$$\|\mathbf{v}_k\|_b \leq \bar{v}, \quad \|\mathbf{u}_k\|_b \leq \bar{u},$$

where \bar{v} and \bar{u} represent the maximum velocity and acceleration input respectively. $\|\cdot\|_b$ denotes some norms according to the platform property, with $b = 2$ and $b = \infty$ denoting the 2-norm and infinity norm, respectively.

Remark 1. *In this paper, we only consider the mission level control of a UAV to achieve the desired inspection trajectory pattern by feeding in acceleration control commands to produce position and velocity outcome, like the linear model (1). We assume that there is a low level autopilot controller on-board the UAV that takes account the nonlinear and coupled dynamic of the platform, and manipulates the physical actuators to achieve the effect of the desired input \mathbf{u} .*

B. Objective

The UAV based façade inspection, as illustrated in Fig. 1, is to generate a proper maneuver pattern based on the façade plane parameter $\bar{\mathbf{n}}_o$ and the inspection pattern, so as to effectively cover the surface of the inspection subject.

- First, to guarantee proper camera observations as well as to avoid collisions, the UAV needs to keep a constant separation distance d_s to the inspection plane, that is

$$\mathbf{n}_o^T \mathbf{p}_k + (d_o - d_s) = 0. \quad (2)$$

- Second, to effectively cover the inspection surface, the UAV trajectory should follow some specific inspection pattern, such as the zig-zag path defined by the d_c and \mathbf{n}_c , in Fig. 1,

$$\mathbf{n}_c^T \mathbf{p}_k - (n_a d_c + d_o) = 0, \quad (3)$$

where \mathbf{n}_c is the inspection path incremental direction, d_o is the initial displacement, and d_c is the displacement between two consecutive inspection rounds. n_a is the counting number of the inspection rounds and increases by one when a round reaches a boundary.

- Additionally, as effective inspection relies on stable camera motion, a reference velocity v_r that provides a trade-off between efficiency and inspection quality is also required, that is

$$\mathbf{n}_p^T \mathbf{v}_k - (-1)^{n_a} v_r = 0, \quad (4)$$

where $\mathbf{n}_p = \mathbf{n}_c \times \mathbf{n}_o$ is the direction of the reference velocity. For the inspection of typical buildings, we can set the inspection direction upward by letting $\mathbf{n}_c = [0 \ 0 \ 1]^T$.

With the definitions and models above, in this paper we consider to solve two consecutive problems, which are 1) plane

parameters \mathbf{n}_o, d_o estimation, and 2) following control of the planar object satisfying Equation (2) to (4), which will be described separately in Section III and Section IV.

III. PLANE ESTIMATION

In this part, the plane pose estimation problem is studied. Specifically, we consider that a camera is installed on the UAV to obtain 2D visual features of the façade plane, then the plane parameters in the camera frame \mathcal{C} , denoted as \mathbf{n}_o^c, d_o^c , are estimated. Finally, based on the pose information of the UAV, the plane parameters in the global frame, \mathbf{n}_o, d_o can be estimated.

A. Plane observer design

To begin with, we simply consider one 3-D point in the camera frame \mathcal{C} , denoted as $\mathbf{X}^c = [X^c, Y^c, Z^c]^T \in \mathbb{R}^3$, projected onto the 2-D image plane as $\mathbf{s} = [x, y]^T \in \mathbb{R}^2$ with the pin-hole model, then the following relationship holds,

$$\frac{1}{Z^c} = -\frac{(\mathbf{n}_o^c)^T}{d_o^c} \begin{bmatrix} x \\ y \\ 1 \end{bmatrix}, \quad (5)$$

where \mathbf{n}_o^c and d_o^c define one plane that the 3-D point belongs to in the camera frame, and Z^c is the depth of the 3-D point in the camera frame.

The relationship between camera motion and pixel dynamics can be expressed with the well-known differential equation (6),

$$\dot{\mathbf{s}} = \mathbf{L} \begin{bmatrix} \mathbf{v}^c \\ \boldsymbol{\omega}^c \end{bmatrix}, \quad (6)$$

where $\mathbf{L} = \begin{bmatrix} -1/Z^c & 0 & x/Z^c & xy & -1-x^2 & y \\ 0 & -1/Z^c & y/Z^c & 1+y^2 & -xy & -x \end{bmatrix}$. $\mathbf{v}^c = [v_x \ v_y \ v_z]^T \in \mathbb{R}^3$ and $\boldsymbol{\omega}^c = [\omega_x \ \omega_y \ \omega_z]^T \in \mathbb{R}^3$ denote the translational and angular velocity of the camera frame respectively.

For more intuitive formulation, let $\boldsymbol{\chi} = -\frac{\mathbf{n}_o^c}{d_o^c} \in \mathbb{R}^3$. Then by substituting equation (5) into equation (6), we have the feature motion expressed in terms of $\boldsymbol{\chi}$ as

$$\begin{bmatrix} \dot{x} \\ \dot{y} \end{bmatrix} = \begin{bmatrix} (xv_z - v_x)\boldsymbol{\chi}^T \bar{\mathbf{p}} + xy\omega_x - (1+x^2)\omega_y + y\omega_z \\ (yv_z - v_y)\boldsymbol{\chi}^T \bar{\mathbf{p}} + (1+y^2)\omega_x - xy\omega_y - x\omega_z \end{bmatrix}. \quad (7)$$

Remark 2. *The above representation $\boldsymbol{\chi} \in \mathbb{R}^3$ is a minimum representation of a 3D plane similar to the closest point approach [28]. The implementation of inverse depth here instead of depth can simplify the modeling of the observer due to the camera model (5). The inverse depth is widely used in camera based applications, such as visual servoing [29], SLAM [30].*

The derivative of the plane parameter $\boldsymbol{\chi}$ based on its definition is

$$\dot{\boldsymbol{\chi}} = -\frac{\dot{\mathbf{n}}_o d_o - \mathbf{n}_o \dot{d}_o}{d_o^2}. \quad (8)$$

The derivatives of \mathbf{n}_o and d_o , by the camera motion \mathbf{v}^c and $\boldsymbol{\omega}^c$, are

$$\dot{\mathbf{n}}_o = [\boldsymbol{\omega}^c]_{\times} \mathbf{n}_o, \quad (9)$$

$$\dot{d}_o = \mathbf{n}_o^c \mathbf{v}^c. \quad (10)$$

Substitute the above equations into (8), the derivative of χ is

$$\dot{\chi} = \chi\chi^T v^c - [\omega^c]_{\times} \chi. \quad (11)$$

Conclusively, the dynamics of the 2-D image feature and planar object parameter can be formulated as

$$\begin{cases} \dot{s} = f_s(s, u) + \Omega^T \chi, \\ \dot{\chi} = f_{\chi}(\chi, p, u), \end{cases} \quad (12)$$

where

$$f_s(s, u) = \begin{bmatrix} xy & -1 - x^2 & y \\ 1 + y^2 & -xy & -x \end{bmatrix} \omega,$$

$$\Omega = \begin{bmatrix} x \\ y \\ 1 \end{bmatrix} [xv_z - v_x \quad yv_z - v_y],$$

$$f_{\chi}(\chi, p, u) = \chi\chi^T v^c - [\omega^c]_{\times} \chi.$$

Define the estimated tracking feature and plane parameter respectively as \hat{s} and $\hat{\chi}$, then the planar object parameter can be estimated with the following observer [12]:

$$\begin{cases} \dot{\hat{s}} = L_{\omega} \omega + \Omega^T \hat{\chi} + H\xi, \\ \dot{\hat{\chi}} = \hat{\chi}\hat{\chi}^T v - [\omega]_{\times} \hat{\chi} + \lambda \Omega \xi, \end{cases} \quad (13)$$

where $\xi = s - \hat{s} \in \mathbb{R}^2$ is the feature tracking error on the image plane. H and λ are the observer gains.

Assumption 1. To simplify the problem, we assume that the motion of the camera can be accurately obtained with perfectly known movement of the UAV and translational relationship between the UAV frame and the camera frame.

With the estimated $\hat{\chi}$, the planar parameters in the camera frame can be calculated as

$$\hat{n}_o^c = \frac{\hat{\chi}}{\|\hat{\chi}\|}, \hat{d}_o^c = \frac{1}{\|\hat{\chi}\|}. \quad (14)$$

The parameters are transferred to the global frame as

$$\begin{bmatrix} n_o^g \\ d_o^g \end{bmatrix} = M^{-T} \begin{bmatrix} n_o^c \\ d_o^c \end{bmatrix}, \quad (15)$$

where n_o^g and d_o^g denote the normal vector and depth in global frame. The superscript g is omitted in the sequel without causing confusion. $M \in SE(3)$ is a matrix of Lie group which is determined by the camera rotation and translation in the global frame [31].

B. Convergence Analysis

Define the error vector of s and χ as $e = [\xi^T, \varepsilon^T]^T$, where $\varepsilon = \hat{\chi} - \chi$, the error dynamics based on the above observer is

$$\begin{cases} \dot{\xi} = -H\xi + \Omega\varepsilon, \\ \dot{\varepsilon} = -\lambda\Omega\xi + g(\varepsilon, v, \omega), \end{cases} \quad (16)$$

where $g(\cdot) \triangleq f_{\chi}(\chi, p, u) - f_{\chi}(\hat{\chi}, p, u)$. According to (11), the term $g(\cdot)$ is a vanishing term w.r.t. the error ε , i.e., $g(\varepsilon) \rightarrow 0$ as $\varepsilon \rightarrow 0$.

Lemma 1. (Persistence of Excitation [12]) The origin of (16) is locally exponentially stable if and only if the following persistency of excitation condition holds:

$$\int_t^{t+T} \Omega(\tau)\Omega^T(\tau)d\tau \geq \beta I_n > 0, \quad \forall t \geq t_0, \quad (17)$$

for some $T > 0$ and $\beta > 0$, with I_n being the $n \times n$ identity matrix.

Given one feature with position $[x, y]^T$ under camera velocity $[v_x, v_y, v_z]^T$, the square matrix $\Omega(t)\Omega^T(t)$ is

$$\Omega(t)\Omega^T(t) = ((xv_z - v_x)^2 + (yv_z - v_y)^2) \begin{bmatrix} x^2 & xy & x \\ xy & y^2 & y \\ x & y & 1 \end{bmatrix}. \quad (18)$$

It's obvious that, for one feature situation, $\text{rank}(\Omega(t)\Omega^T(t)) \leq 1$ and $\chi \in \mathbb{R}^3$ cannot be estimated. By implementing multiple features, we have the following conclusion.

Lemma 2 (Convergence conditions). Consider m features in the observer, the PE condition can be satisfied with the following conditions:

- There exists a minimum set of 4 feature points satisfying that any three are not collinear,
- and the control velocity is not zero.

Proof. Define $\bar{\Omega} = [\Omega_1, \dots, \Omega_m]$ as the stacked matrix of m features. Then the squared matrix for m features are

$$\bar{\Omega}\bar{\Omega}^T = \sum_{i=1}^m \Omega_i\Omega_i^T = [\alpha_1 \bar{s}_1 \quad \alpha_2 \bar{s}_2 \quad \dots \quad \alpha_m \bar{s}_m] \begin{bmatrix} \alpha_1 \bar{s}_1^T \\ \alpha_2 \bar{s}_2^T \\ \vdots \\ \alpha_m \bar{s}_m^T \end{bmatrix}, \quad (19)$$

where $\alpha_i = \sqrt{(x_i v_z - v_x)^2 + (y_i v_z - v_y)^2}$, and $\bar{s}_i = [x_i, y_i, 1]^T = \frac{1}{Z_i} X_i$.

We consider a more strict PE condition by enforcing $\bar{\Omega}\bar{\Omega}^T \geq \beta I_3$, or equivalently

$$\text{rank}([\alpha_i \frac{1}{Z_i} X_1 \quad \alpha_2 \frac{1}{Z_2} X_2 \quad \dots \quad \alpha_m \frac{1}{Z_m} X_m]) = 3. \quad (20)$$

To guarantee that, we need at least three independent column vectors X_i in the matrix (20), or equally, there are at least 3 points on the image plane which are neither coincident nor collinear, and, the corresponding α_i is not zero. Now we investigate the situations that make $\alpha_i = 0$.

- $v_x = v_y = v_z = 0$, which means the camera is stationary;
- $x_i = v_x/v_z, y_i = v_y/v_z, v_z \neq 0$, which means the camera is moving on the line connecting the feature X_i and the camera center.

For the first case, all the elements $\alpha_i \frac{1}{Z_i} X_i$ are zeros, and therefore the rank of (20) is zero. For the second case, assume there is a feature i that satisfies $\alpha_i = 0$, then for all other $m-1$ features j that do not coincide with i , $\alpha_j \neq 0$.

Finally, we can conclude that with the sufficient conditions proposed, the $\text{rank}(\bar{\Omega}\bar{\Omega}^T) \equiv 3$ with an arbitrary non-zero camera movement. \square

As stated in [13], the convergence rate of the error system (16) is related to the minimum eigenvalue of the matrix $\Omega\Omega^T$, which is decided by the velocity v and features s .

Lemma 3 (Convergence rate). *Consider a scenario where the PE condition is satisfied, and given a reference direction of the moving camera, the convergence rate or the minimum eigenvalue of the matrix, denoted by λ_{min} , is*

- proportional to the square norm of velocity, $\lambda_{min} \propto \|\mathbf{v}\|^2$,
- a monotonic function with regard to the features set, namely, given two feature set $A \subseteq B$, $\lambda_{min}(A) \leq \lambda_{min}(B)$.

Proof. The first property is straightforward based on the definition of the square matrix (19). Denote the square matrix $\bar{\Omega}\bar{\Omega}^T$ corresponding to two different non-empty feature sets A and B as Ξ_A and Ξ_B respectively. Based on (19), we have Ξ_A , Ξ_B and $\Xi_{B \setminus A}$ are all symmetric matrices. According to the Rayleigh-Ritz method [32], the minimal eigenvalue of a symmetric matrix M satisfies

$$\lambda_{min}(M) = \min_{\mathbf{x} \neq 0} \frac{\mathbf{x}^T M \mathbf{x}^T}{\mathbf{x}^T \mathbf{x}^T}, \quad (21)$$

where \mathbf{x} is a vector of the same dimension.

As $\Xi_B = \Xi_A + \Xi_{B \setminus A}$, the minimum eigenvalue of matrix Ξ_B is

$$\begin{aligned} \lambda_{min}(\Xi_B) &= \lambda_{min}(\Xi_B + \Xi_{B \setminus A}) \\ &= \min \left(\frac{\mathbf{x}^T \Xi_A \mathbf{x}^T}{\mathbf{x}^T \mathbf{x}^T} + \frac{\mathbf{x}^T \Xi_{B \setminus A} \mathbf{x}^T}{\mathbf{x}^T \mathbf{x}^T} \right) \\ &\geq \min_{\mathbf{x} \neq 0} \frac{\mathbf{x}^T \Xi_A \mathbf{x}^T}{\mathbf{x}^T \mathbf{x}^T} + \min_{\mathbf{x} \neq 0} \frac{\mathbf{x}^T \Xi_{B \setminus A} \mathbf{x}^T}{\mathbf{x}^T \mathbf{x}^T} \\ &= \lambda_{min}(\Xi_A) + \lambda_{min}(\Xi_{B \setminus A}). \end{aligned} \quad (22)$$

Furthermore, according to the definition of the square matrix, the matrix Ξ_A and Ξ_B and $\Xi_{B \setminus A}$ are all positive semidefinite, which means $\lambda_{min}(\Xi_{B \setminus A}) \geq 0$, then we can have the conclusion $\lambda_{min}(\Xi_B) \geq \lambda_{min}(\Xi_A)$. \square

Based on Lemma 2 and 3, we can conclude that, in spite that the convergence is guaranteed under very mild condition of the number of features, the convergence rate is positively correlated to the feature richness. To guarantee the stability and smoothness of the subsequent plane following control, we should adopt as many features as possible in the observer.

C. Connected planes estimation

In a practical scenario with off-the-shelf camera sensors, the derivatives of the feature points are approximated with feature displacement between consecutive frames. Due to the limited field of view of a typical camera, the feature set \mathbf{s} in the observer is dynamically updated with the motion of camera. To realize continuous estimation on consecutive planes, the above observer, denoted as *PE_Observer* is implemented in Algorithm 1.

Algorithm 1: Plane parameters estimation

Init: Observer gains α, β ;
Plane estimate $\hat{\chi}_0$, feature set $\hat{\mathbf{s}}_0 = Null$;

```

1 while  $k \geq 0$  do
2   Obtain one image from camera and extract one set
   of features  $\mathcal{S}_k$ ;
3   Obtain the camera velocity and rotation velocity
    $\mathbf{v}_k, \boldsymbol{\omega}_k$ ;
4   Run feature matching between  $\mathcal{S}_k$  and  $\mathcal{S}_{k-1}$ ;
5   for  $\mathbf{s}_j \in \mathcal{S}_k$  do
6     if  $\mathbf{s}_j$  matches  $\mathbf{s}_l \in \mathcal{S}_{k-1}$  then
7        $\hat{\mathbf{s}}_j = \hat{\mathbf{s}}_l$ ;
8     else
9        $\hat{\mathbf{s}}_j = \mathbf{s}_j$ ;
10    end
11  end
12   $\hat{\chi}_k, \hat{\mathbf{S}}_k \leftarrow PE\_Observer(\hat{\chi}_k, \hat{\mathbf{S}}_k, \mathbf{v}_k, \boldsymbol{\omega}_k, \alpha, \beta)$ ;
13 end

```

IV. PLANE FOLLOWING

A. MPC based plane following

For the plane following problem described in Section II-B, we can formulate an objective function as

$$\begin{aligned} \min_{\mathbf{u}} \sum_{t=1}^H & (c_1 \|\mathbf{n}_o^T \mathbf{p}_{k+t} - d_{ref}\|^2 + c_2 \|\mathbf{n}_c^T \mathbf{p}_{k+t} - z_{ref}\|^2 \\ & + c_3 \|\mathbf{n}_p^T \mathbf{v}_{k+t} - v_{ref}\|^2) + \|\mathbf{u}_{k+t-1}\|_R^2, \end{aligned} \quad (23)$$

where $d_{ref} = d_c - d_o$, $z_{ref} = n_a d_c + d_0$, and $v_{ref} = (-1)^{n_a} v_r$.

Remark 3. *The parameter n_a is to count the inspection round of the whole mission process. When a boundary or a potential collision is detected, it automatically adds one, which results in that the reference z_{ref} adds by a constant displacement d_c , and reverses the direction of the velocity v_{ref} . Although the proposed method counts on n_a , we only consider the estimation and path planning of the inspection area and the detection of boundaries is out of the scope of this paper.*

By transforming the position of the platform into a homogeneous coordinate, i.e. $\bar{\mathbf{x}} = [x \ y \ z \ 1 \ v_x \ v_y \ v_z]^T$, the objective function can be further rewritten as a constant reference tracking problem as

$$J = \sum_{t=1}^H \|\mathbf{C} \bar{\mathbf{x}}_{k+t} - \mathbf{c}_r\|_Q^2 + \|\mathbf{u}_{k+t-1}\|_R^2, \quad (24)$$

where $\mathbf{C} \in \mathbb{R}^{3 \times 7}$ is a matrix based on the plane vector, and \mathbf{c}_r is a constant reference vector, respectively as

$$\mathbf{C} = \begin{bmatrix} \mathbf{n}_o^T & d_o & \mathbf{0}_{1 \times 3} \\ \mathbf{n}_c^T & 0 & \mathbf{0}_{1 \times 3} \\ \mathbf{0}_{1 \times 3} & 0 & \mathbf{n}_c \times \mathbf{n}_o^T \end{bmatrix}, \quad \mathbf{c}_r = \begin{bmatrix} d_{ref} \\ z_{ref} \\ v_{ref} \end{bmatrix}. \quad (25)$$

The weight matrix $Q = \text{diag}([c_1 \ c_2 \ c_3])$.

Problem 1. By incorporating the dynamics of the system, the problem can be formulated as a typical MPC based reference tracking problem,

$$\min_{\mathbf{u}_{k:k+H}} J(\mathbf{x}_{k:k+H}, \mathbf{u}_{k:k+H-1}) \quad (26a)$$

$$\text{s.t. } \mathbf{x}_{k+t} = \mathbf{A}\mathbf{x}_{k+t-1} + \mathbf{B}\mathbf{u}_{k+t-1}, \quad (26b)$$

$$\|\mathbf{v}_{k+t}\| \leq \bar{v}, \quad (26c)$$

$$\|\mathbf{u}_{k+t}\| \leq \bar{u}, \quad (26d)$$

$$\mathbf{C}_k \bar{\mathbf{x}}_{k+H} - \mathbf{c}_r \in \mathcal{E}. \quad (26e)$$

The last term (26e) is the terminal condition to guarantee the close loop tracking performance, and \mathcal{E} is the corresponding terminal set. The controller above is denoted as *PF_MPC* in the following parts.

Remark 4. Although not required by the plane observer, we consider to control the camera optical axis to be roughly aligned with the normal vector of the estimated plane to obtain better inspection details. For a camera rigidly connected to a UAV, this alignment can be achieved at least on the $x-y$ plane by sending a yaw command according to plane estimation to the autopilot of the UAV. For a gimbaled camera, the alignment can be realized in 3D by controlling the gimbals angles.

B. Recursive Feasibility

Assumption 2. There exists a finite receding horizon H satisfying that, for any \mathbf{x}_0 and $\hat{\mathbf{C}}_0$ that belong to the initial sets $\hat{\mathbf{C}}_0 \in \mathcal{C}_0$ and $\mathbf{x}_0 \in \mathcal{X}_0$ respectively, the solution for the MPC Problem 1 is feasible.

With the feasibility Assumption 2, we denote the optimal control sequence at time k as $\mathbf{U}_k^* = [(\mathbf{u}_{k|k}^*)^T \ (\mathbf{u}_{k+1|k}^*)^T \ \cdots \ (\mathbf{u}_{k+H-1|k}^*)^T]^T$, which satisfies the terminal condition $\hat{\mathbf{C}}_0 \bar{\mathbf{x}}_{k+H} - \mathbf{c}_r \in \mathcal{E}$. Next, we need to find a feasible solution at time $k+1$. Based on the optimal control sequence \mathbf{U}_k^* , we compose one control sequence as $\mathbf{U}'_{k+1} = [(\mathbf{u}_{k+1|k}^*)^T \ (\mathbf{u}_{k+2|k}^*)^T \ \cdots \ (\mathbf{u}_{k+H-1|k}^*)^T \ (\mathbf{u}'_{k+H|k+1})^T]^T$. Then if $\mathbf{u}'_{k+H|k+1}$ satisfies the terminal condition

$$\hat{\mathbf{C}}_{k+1}(\mathbf{A}\bar{\mathbf{x}}_{k+H|k} + \mathbf{B}\mathbf{u}'_{k+H|k+1}) - \mathbf{c}_r \in \mathcal{E}, \quad (27)$$

and constraints (26c,26d), \mathbf{U}'_{k+1} is one feasible solution. Apparently, when the estimator is stable, namely for a large enough k , $\hat{\mathbf{C}}_{k+1} = \hat{\mathbf{C}}_k = \mathbf{C}_k$, then based on the definition of \mathbf{C} , $\hat{\mathbf{C}}_{k+1} \mathbf{A}\bar{\mathbf{x}}_{k+H|k} = \hat{\mathbf{C}}_k \bar{\mathbf{x}}_k - \mathbf{c}_r \in \mathcal{E}$, i.e. the terminal condition can always be satisfied by letting $\mathbf{u}'_{k+H|k} = \mathbf{0}$, which means the solution is always feasible when the estimator is stable.

Otherwise, let $\hat{\mathbf{C}}_{k+1} = \hat{\mathbf{C}}_k + \Delta\mathbf{C}$ and we can obtain a control input that guarantees (27) as

$$\mathbf{u} = \left((\Delta\mathbf{C} + \hat{\mathbf{C}}_k) \mathbf{B} \right)^{-1} \Delta\mathbf{C} \mathbf{A} \mathbf{x}, \quad (28)$$

where

$$\Delta\mathbf{C} = \begin{bmatrix} \Delta\mathbf{n}_o & \Delta d_o & \mathbf{0}_{1 \times 3} \\ \mathbf{0}_{1 \times 3} & 0 & \mathbf{0}_{1 \times 3} \\ \mathbf{0}_{1 \times 3} & 0 & \Delta\mathbf{n}_o \times \mathbf{n}_c \end{bmatrix}. \quad (29)$$

The control input (28) may violate the control input constraint for a large change $\Delta\mathbf{C}$. In order to guarantee the control feasibility, an estimation update strategy for the sampling of $\hat{\chi}$ is designed to limit $\Delta\mathbf{C}$ as

$$\hat{\chi}_{s,k+1} = \hat{\chi}_{s,k} + \gamma(\hat{\chi}_{(k+1)\delta t_s} - \hat{\chi}_{s,k}), \quad (30)$$

where δt_s is the sampling time interval, $\gamma \in [0, 1]$ is an update step factor and should be adaptively changed so that the control input (28) is always feasible. Denote \mathbf{C} corresponding to $\hat{\chi}_{s,k}$ as $\hat{\mathbf{C}}_{s,k}$, then $\hat{\mathbf{C}}_{s,k+1}$ and $\Delta\mathbf{C}_{s,k}$ can be treated as functions of γ

$$\hat{\mathbf{C}}_{s,k+1}(\gamma) = \hat{\mathbf{C}}_{s,k} + \Delta\mathbf{C}_{s,k}(\gamma). \quad (31)$$

The largest feasible γ , denoted as $\bar{\gamma}$, can be calculated numerically by combining (30) with the below equation :

$$\|\mathbf{u}\| = \left\| \left((\Delta\mathbf{C}_{s,k} + \hat{\mathbf{C}}_{s,k}(\gamma)) \mathbf{B} \right)^{-1} \Delta\mathbf{C}_{s,k}(\gamma) \mathbf{A} \bar{\mathbf{x}} \right\| = \bar{u}. \quad (32)$$

The adaptive step size is $\gamma = \min\{1, \bar{\gamma}\}$. Obviously, when the difference between the current estimate from observer χ and the last sampled estimate χ_s is so large that the control input calculated directly from (28) is not feasible, $\gamma < 1$ serves as a discount factor, and when the tracking error becomes small enough, $\gamma = 1$.

Lemma 4. Based on the proposed plane observer as well as the update rule (30), the sampled $\hat{\chi}_s$ ultimately converges to the true planar parameters χ , and during the updating process, the MPC is recursively feasible.

Proof. Based on the updating rule (30), we have

$$\Delta\hat{\chi}_{s,k} \triangleq \hat{\chi}_{s,k+1} - \hat{\chi}_{s,k} = \gamma(\hat{\chi}_{(k+1)\delta t_s} - \hat{\chi}_{s,k}). \quad (33)$$

For a large enough sampling time instance k' , the estimation from the proposed plane observer converges to the true value, $\hat{\chi}_{k'\delta t_s} \rightarrow \chi$, therefore for $k > k'$, the error between the true value and the sampled value evolves as

$$(\hat{\chi}_{s,k+1} - \chi) = (1 - \gamma)(\hat{\chi}_{s,k} - \chi). \quad (34)$$

According to the definition of γ , when $\hat{\chi}_{s,k} - \chi$ is large, $0 < \gamma < 1$, and the true value tracking error monotonically decreases. When the tracking error becomes small enough at time instance $k'' > k'$ so that the feasibility of (28) is guaranteed, $\gamma = 1$, and $\hat{\chi}_{s,k''+1} - \chi = 0$, namely the sampled $\hat{\chi}_{s,k}$ converges to the true planar parameters χ .

Obviously, if there exists a feasible solution at time k , then according to the update rule in (30), the terminal condition at time $k+1$ can always be satisfied given a proper control, as in (27), which means that there is always a feasible solution at $k+1$. The recursive feasibility is proved. \square

Apparently, the adaptive updating step size slows down the convergence rate of the planar objective tracking, to an acceptable level of the platform maneuverability.

C. Tracking stability

To investigate the stability of the proposed MPC controller, we define the planar object tracking error as

$$\mathbf{e} = \mathbf{C}\bar{\mathbf{x}} - \mathbf{c}_r, \quad (35)$$

which corresponds to the first part of the objective function (24).

Theorem 1. *Based on the proposed planar object estimator (13) and its corresponding discrete time update rule (30), and given that the initial state satisfies the feasible Assumption 2, the proposed receding horizon controller can properly track the reference \mathbf{c}_r , i.e. the tracking error \mathbf{e} defined above is asymptotically stable.*

Proof. According to the feasibility Assumption (2), the solution of Problem (1) is feasible for a state $\mathbf{x}_k \in \mathcal{X}$. Denote the optimal solution at time instance k as $\mathbf{U}_k^* = [(\mathbf{u}_{k+1|k}^*)^T \ (\mathbf{u}_{k+2|k}^*)^T \ \cdots \ (\mathbf{u}_{k+H-1|k}^*)^T]^T$. The corresponding objective function is

$$J^*(k) = \sum_{i=1}^H \|\hat{\mathbf{C}}_k \bar{\mathbf{x}}_{k+i|k}^* - \mathbf{c}_r\|_Q^2 + \|\mathbf{u}_{k+i-1|k}^*\|_R^2. \quad (36)$$

Similar to Section IV-B, we have one feasible solution at time $k+1$ as $[(\mathbf{u}'_{k+1|k+1})^T \ (\mathbf{u}'_{k+2|k+1})^T \ \cdots \ (\mathbf{u}'_{k+H|k+1})^T]^T = [(\mathbf{u}_{k+1|k}^*)^T \ (\mathbf{u}_{k+2|k}^*)^T \ \cdots \ (\mathbf{u}'_{k+H|k+1})^T]^T$. Using the terminal constraint, we have $\hat{\mathbf{C}}_k \bar{\mathbf{x}}_{k+H=|k}^* - \mathbf{c}_r \in \mathcal{E}$. Letting $\mathbf{u}'_{k+H|k+1} = \mathbf{0}$, we have $\hat{\mathbf{C}}_k \bar{\mathbf{x}}_{k+H+1|k}^* = \mathbf{c}_r$. Thanks to the local convergence property of the estimator, for $k \rightarrow \infty$, $\hat{\mathbf{C}}_k \rightarrow \mathbf{C}$. Then we have the objective function based on the feasible solution as

$$\begin{aligned} J'(k+1) &= \sum_{i=2}^{H+1} \|\hat{\mathbf{C}}_{k+1} \mathbf{x}'_{k+i|k+1} - \mathbf{c}_r\|_Q^2 + \|\mathbf{u}'_{k+i|k+1}\|_R^2 \\ &= \sum_{i=2}^H \|\hat{\mathbf{C}}_{k+1} \mathbf{x}_{k+i|k}^* - \mathbf{c}_r\|_Q^2 + \|\mathbf{u}_{k+i|k}^*\|_R^2. \end{aligned} \quad (37)$$

Hence,

$$\begin{aligned} J^*(k+1) - J^*(k) &\leq J'(k+1) - J^*(k) \\ &= -\|\hat{\mathbf{C}}_k \bar{\mathbf{x}}_k - \mathbf{c}_r\|_Q^2 - \|\mathbf{u}_{k|k}\|_R^2 \leq 0. \end{aligned} \quad (38)$$

As $\hat{\mathbf{C}}_k \rightarrow \mathbf{C}$ as $t \rightarrow 0$, we can conclude that the tracking error defined above is asymptotically stable. \square

D. Plan following under connected planes

Based on the above estimator and controller, an algorithm that enables concatenated planes following is described in Algorithm 2.

V. SIMULATIONS

This subsection presents numerical simulations based on MATLAB [33] and the Machine Vision Toolbox [34], to test the performance of the proposed plane estimation and plane following methods. Specifically, the simulation scenario is described as a projective camera model observing synthetic features so as to estimate and follow the planes.

Algorithm 2: Plane Follower

Init: Inspection parameters: v_r, d_s, n_a, d_c ;
MPC parameters: Q, R, H , initial state $\mathbf{x}_0, \mathbf{C}_0$;

- 1 **while** not stop inspection **do**
- 2 Subscribe plane estimation information from Algorithm 1;
- 3 Update $\hat{\chi}_{s,k}$ according to (30);
- 4 Calculate $\hat{\mathbf{C}}_{s,k}$ according to (14),(15),(25);
- 5 **if** Is arrived at boundary **then**
- 6 Update the reference \mathbf{c}_r according to (3),(4);
- 7 $a \leftarrow a + 1$
- 8 **end**
- 9 Calculate the MPC controller
- 10 $\mathbf{u}_{k:k+H-1}, \mathbf{x}_{k+1:k+H} \leftarrow PF_MPC(\mathbf{x}_k, \mathbf{C}_k)$;
- 11 Execute \mathbf{u}_k .
- 11 **end**

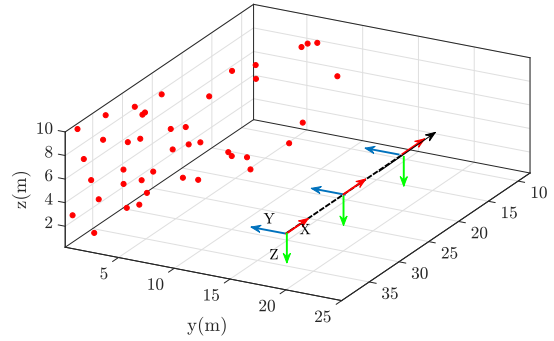


Figure 2. The simulation scenario with synthetic features in red dot and camera pose in blue.

A. Plane Estimation

In the first simulation scenario, the performance of the plane estimator based on different settings, such as different translational velocities and different level of feature richness, are investigated. The synthetic 3-D feature points are randomly placed on the plane determined by the plane normal vector $\mathbf{n}_o = [-0.2425, -0.9701, 0]^T$, and feature depth $d_o = 9.7011$. One camera with limited horizontal FOV 46° and vertical FOV 38° , is initialized with the transformation matrix

$$\mathbf{M}(0) = \begin{bmatrix} -1 & 0 & 0 & 40 \\ 0 & 0 & -1 & 20 \\ 0 & -1 & 0 & 5 \\ 0 & 0 & 0 & 1 \end{bmatrix}.$$

The observer gains are set as $H = 12\mathbf{I}$, and $\lambda = 0.95\mathbf{I}$. The results of 40 seconds simulation based on the proposed observer running at 10 Hz is plotted in Figure 3. In this simulation, 100 random features are simulated, and the camera is moving with a constant velocity $\mathbf{v} = [0.5; 0; 0]$. Fig.3 shows the convergence behavior of the estimation for both plane normal vector and plane depth.

Moreover, the effect of the translational velocity and the number of features n_s on the convergence rate of the estimation is investigated. The plane normal vector estimation error

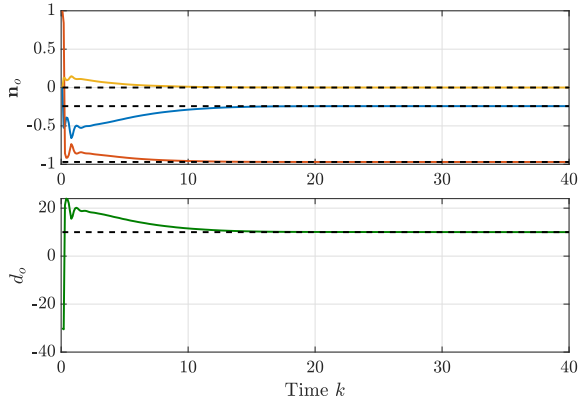


Figure 3. The plane vectors \mathbf{n}_o , and d_o in colors w.r.t to ground-truth in black dash-lines.

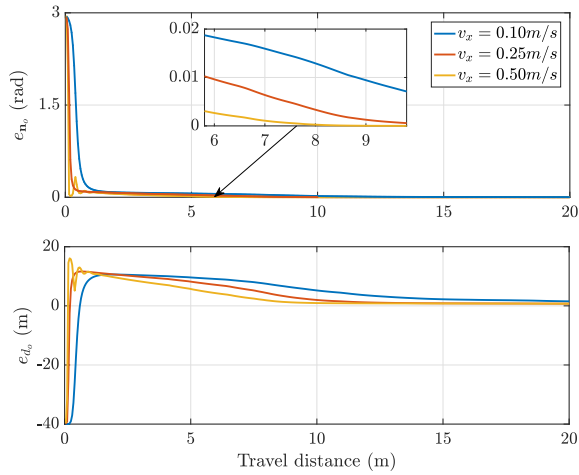


Figure 4. The errors $e_{\mathbf{n}_o}$ and e_{d_o} under different translation velocities $v_x = 0.1\text{m/s}, 0.25\text{m/s}, 0.5\text{m/s}$ respectively.

and the estimation error of depth d_o are defined respectively as

$$e_{\mathbf{n}_o} = \cos^{-1}(\mathbf{n}_o^T \hat{\mathbf{n}}_o), \quad e_{d_o} = d_o - \hat{d}_o.$$

The evolutions of the error under different translational velocity $v_x = 0.1\text{m/s}, 0.25\text{m/s}, 0.5\text{m/s}$ are plotted in Figure 4, which shows that faster movement results in a faster convergence rate. Similarly, the evolution of the errors under different feature numbers are plotted in Figure 5, which shows that the errors converge to zero faster as more features are implemented in the observer. The above two results are consistent with the conclusions of Lemma 3.

Finally, a comparative study of the proposed method along with a typical EKF based estimator (EKF) and a homography-constrained method (Homo.) [14] is provided under a similar scenario as above. Specifically, the covariance of the measurement noise of \mathbf{s} is set as $\Sigma_s = \text{diag}([0.001, 0.001])$. The results of one trial using the three methods are plotted in Fig. 6. Additionally, 100 Monte-Carlo trials are carried out, and the averaged estimation errors with different methods are plotted in Figure 7. From Fig. 6 and Fig. 7, it's apparent that the convergence rate of the proposed method is faster compared to the EKF, and the homography based method can achieve the fastest convergence rate. Nevertheless, the homography

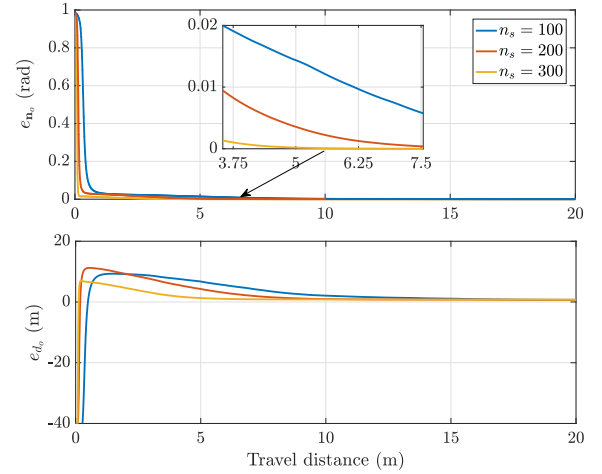


Figure 5. The errors $e_{\mathbf{n}_o}$ and e_{d_o} under different feature richness, with $n_s = 100, 200, 300$ respectively.

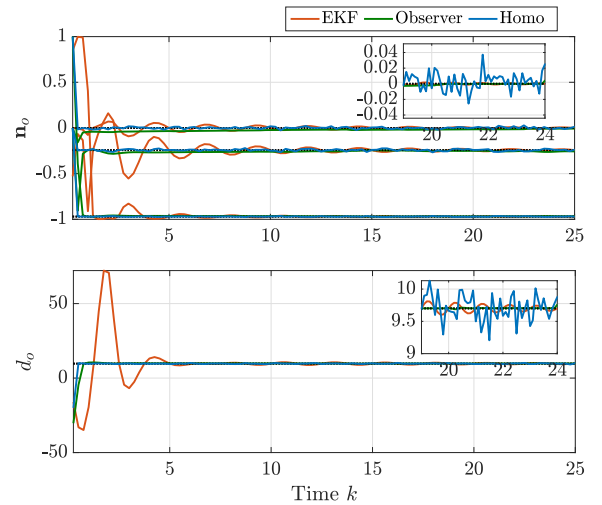


Figure 6. The estimation result of the proposed result v.s. an EKF estimator and the homography based method [14].

decomposition method only relies on image correspondences and is very sensitive to measurement noise, as shown in the amplified sub-figures in Fig. 6. The oscillation of estimation may produce unwanted plane following behavior. On the contrary, the EKF and proposed estimator recursively estimate the depth of the plane, and therefore can achieve much smoother estimation and plane following results.

B. Plane Following

The plane following based on Algorithm 2 is simulated here. Specifically, we consider the continuous following of two connected planes, with the plane parameters denoted respectively as $\bar{\mathbf{n}}_{o1} = [-0.2425, -0.9701, 0, 9.7011]$, and $\bar{\mathbf{n}}_{o2} = [-0.9701, -0.2425, 0, 9.7011]$. The plane following parameters are set as $d_s = 10\text{m}, v_{ref} = 1\text{m/s}$. The inspection pattern is set as $d_0 = 5, d_c = 2\text{m}$. The UAV/Camera velocity and acceleration constraints are set respectively as $\|\mathbf{v}\|_\infty = 3\text{m/s}$ and $\|\mathbf{u}\|_\infty = 0.5\text{m/s}^2$.

The plane following trajectory is plotted in Fig. 8 which indicates that proper path following/inspection behavior is

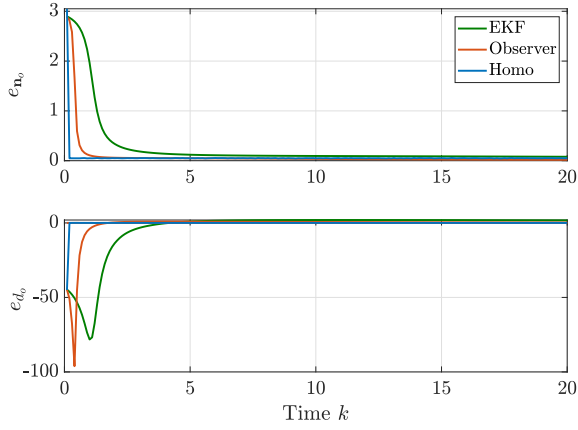


Figure 7. The errors e_{n_o} and e_{d_o} of the proposed method v.s. an EKF estimator and the homograph based method [14] in 100 Mento-Carlo simulations.

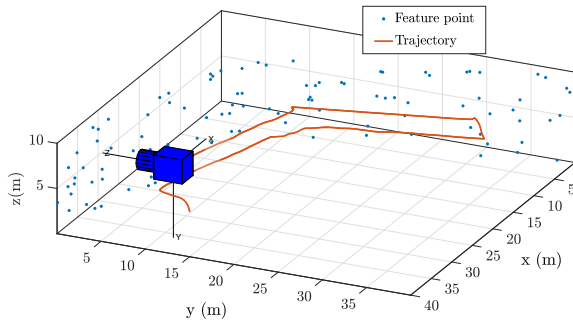


Figure 8. The plane following trajectory w.r.t two connected planes.

achieved. The corresponding velocity and control input are plotted in Figure 9. The estimation results during the path following process is provided in Fig. 10, which indicates that the proposed method can effectively estimate the plane parameters and quickly responds to the plane changes. In addition, the sampling strategy (30), although leading to some latency, can effectively guarantee the feasibility of the proposed controller by providing smoother estimation results. Finally, the performance, i.e. the path following error, defined in (35), is plotted in Figure 11. Conclusively, the proposed estimation and control methods can effectively fulfill the inspection task.

VI. EXPERIEMENTS

In this section, the proposed plane estimation and following methods are tested based on field experiment trials.

A DJI M100 quadrotor carrying an ob-board camera as shown in Fig. 12 is implemented to inspect a building. For safety and comparison purpose, an on-board LiDAR is also installed to provide collision avoidance function. Due to its high range measurement accuracy, around $0.015 \text{ m} \sim 0.1 \text{ m}$, the LiDAR also serves as the ground truth for the path estimation and path following. The software flow of the experiment system is given in Fig. 13. Besides the inspection Algorithm 1 and 2, the VINS-mono package [35] is also implemented to provide the odometry information of the UAV. The interaction

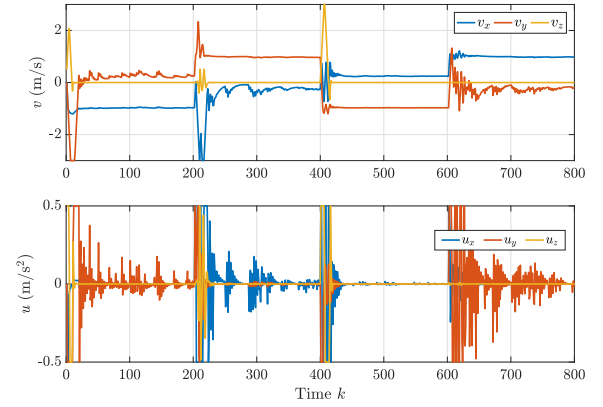


Figure 9. The velocity and control output of the plane following.

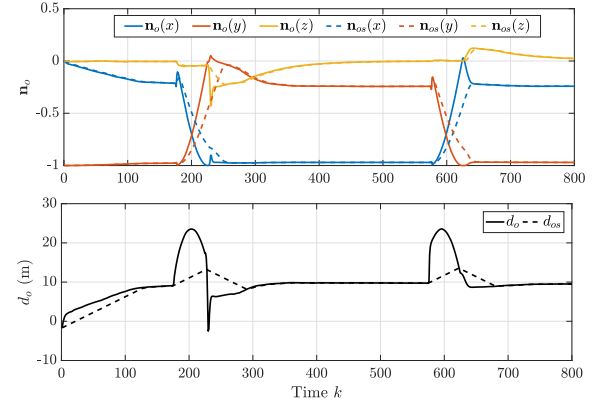


Figure 10. The plane parameters estimation with the original estimation in solid lines and the sampled according to (30) in dashed lines.

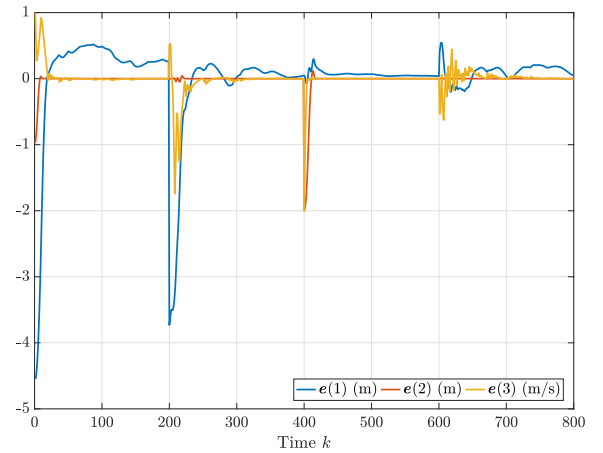


Figure 11. The plane following error e defined in (35).

between the functional modules and the platform is through the DJI onboard SDK [36].

In the inspection task, the inspected building is shown as Figure 14. The separation distance is $d_s = 7.5\text{m}$, and the inspection pattern is specified with $d_0 = 4\text{m}$, and $d_c = 2\text{m}$. For safety purpose, horizontal operation boundaries are set as $p_y \in [0, 10]$.

During the inspection process, the sampled estimation of the building plane \hat{n}_{os} and \hat{d}_{os} is shown in Fig. 15. For comparison purpose, the actual separation distance of the UAV trajectory to the building measured from the on-board LiDAR is also plotted. The corresponding estimation errors, expressed with e_{n_o} and e_{d_o} , are plotted in Fig. 16, which shows that the errors of the estimation are within an acceptable level, $e_{n_o} < 0.2$ rad, and $e_{d_o} < 0.2$ m.

The inspection trajectory of the quadrotor is shown in Fig. 14 with generated point cloud¹, which demonstrates that a proper inspection behavior is achieved. The corresponding velocity and control input are plotted in Fig. 17 and 18, respectively. To further investigate the plane following performance, the plane path following error defined in (35) is plotted in Fig. 19. As indicated in Fig. 19, the tracking errors of the separation distance, displacement, and reference velocity are all within acceptable bounds. Note that the plane estimation and path following also depend on the odometry information provided by the VINS-mono, as shown in (15), therefore the errors of plane estimation in Fig. 15 and path following in Fig. 19 also include the uncertainty of the odometry.



Figure 12. The DJI M100 platform with on-board sensors (cameras, LiDAR) and computer.

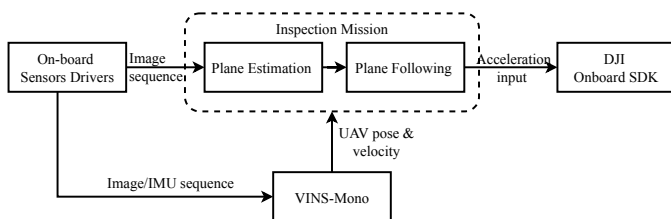


Figure 13. The software & data flow of the experiment platform for inspection task.

VII. CONCLUSION

In this paper, an inspection task, which is formulated as on-line plane estimation and plane following control, is consid-

¹The point cloud is generated offline using recorded data from the LiDAR and the A-LOAM mapping package <https://github.com/HKUST-Aerial-Robotics/A-LOAM>.

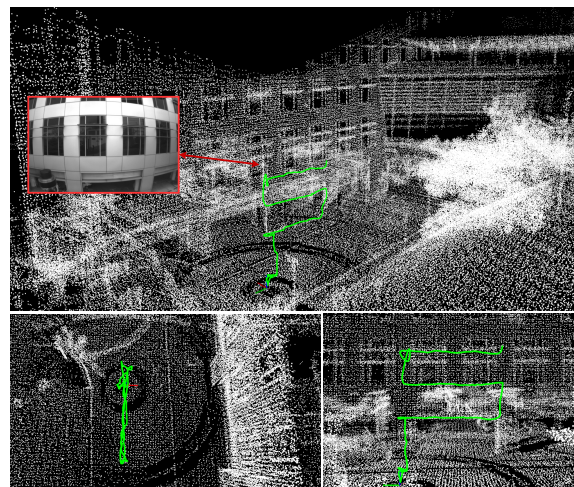


Figure 14. The inspection trajectories (green curves) w.r.t. a building (white point cloud).

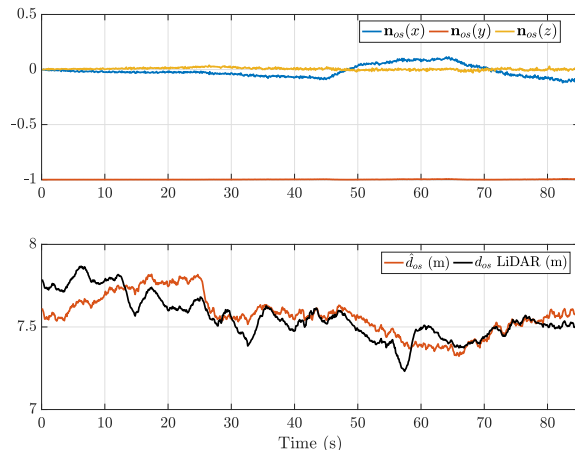


Figure 15. The sampled plane parameters estimation \hat{n}_{os} and \hat{d}_{os} , compared to the separation distance provided by d_s LiDAR.

ered. First, a vision based adaptive plane parameters observer is proposed, which can realize stable plane estimation under very mild conditions. Next, an MPC based plane follower that can automatically integrate the inspection references is designed. The feasibility and stability properties of the controller are also investigated. The effectiveness of the proposed plane estimation and following are verified and validated by simulations and experiments.

In the future, the functional completeness will be further strengthened by integrating inspection boundary detection and collision avoidance so as to fulfill practical inspection tasks.

REFERENCES

- [1] G. Cai, J. Dias, and L. Seneviratne, "A survey of small-scale unmanned aerial vehicles: Recent advances and future development trends," *Unmanned Systems*, vol. 2, no. 02, pp. 175–199, 2014.
- [2] D. Roca, S. Lagüela, L. Díaz-Vilariño, J. Armesto, and P. Arias, "Low-cost aerial unit for outdoor inspection of building façades," *Automation in Construction*, vol. 36, pp. 128–135, 2013.
- [3] X. Peng, H. Zhu, J. Feng, C. Shen, H. Zhang, and J. T. Zhou, "Deep clustering with sample-assignment invariance prior," *IEEE Transactions on Neural Networks and Learning Systems*, 2019.

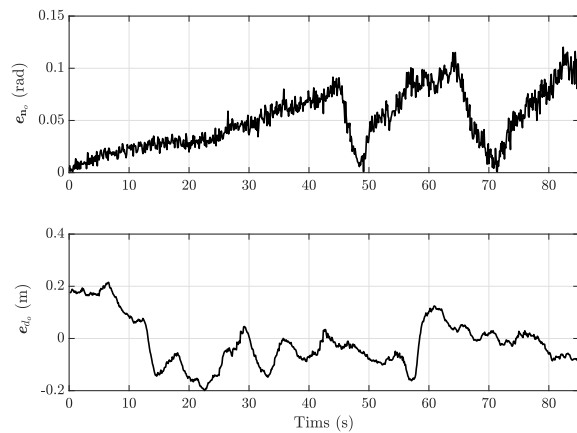


Figure 16. The plane estimation error, the normal vector estimation error e_{n_o} and the depth estimation error e_{d_o} .

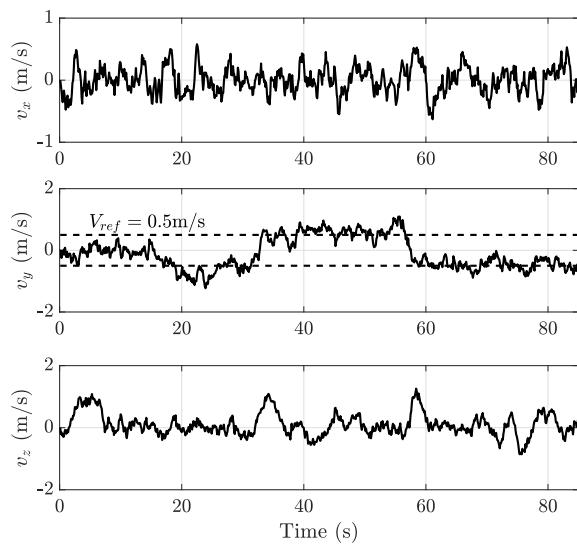


Figure 17. The velocity of the inspection trajectory, with $v_r = 0.5\text{m/s}$.

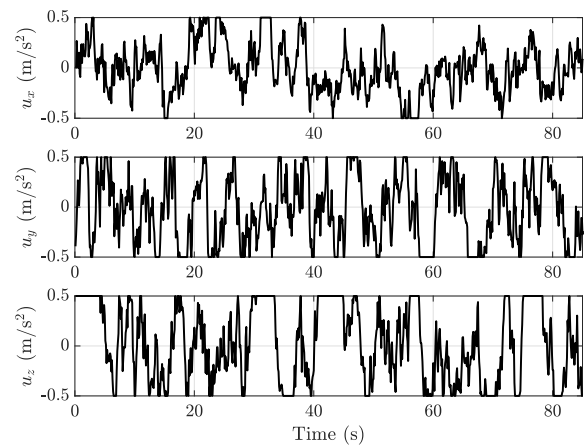


Figure 18. The control \mathbf{u} with constraints $\|\mathbf{u}\|_\infty \leq 0.5\text{m/s}^2$.

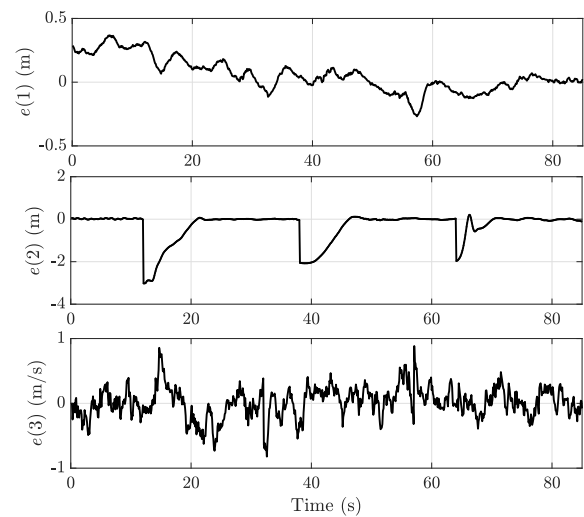


Figure 19. The plane path following errors \mathbf{e} , include separation distance error $e(1)$, round displacement error $e(2)$, and velocity error $e(3)$.

[4] X. Peng, J. Feng, S. Xiao, W.-Y. Yau, J. T. Zhou, and S. Yang, "Structured autoencoders for subspace clustering," *IEEE Transactions on Image Processing*, vol. 27, no. 10, pp. 5076–5086, 2018.

[5] D. Zhou, Y. Dai, and H. Li, "Ground-plane-based absolute scale estimation for monocular visual odometry," *IEEE Transactions on Intelligent Transportation Systems*, vol. 21, no. 2, pp. 791–802, Feb 2020.

[6] T. Lee, S. Lim, S. Lee, S. An, and S. Oh, "Indoor mapping using planes extracted from noisy rgb-d sensors," in *2012 IEEE/RSJ International Conference on Intelligent Robots and Systems*, Oct 2012, pp. 1727–1733.

[7] A. Asvadi, C. Prevedida, P. Peixoto, and U. Nunes, "3d lidar-based static and moving obstacle detection in driving environments: An approach based on voxels and multi-region ground planes," *Robotics and Autonomous Systems*, vol. 83, pp. 299–311, 2016.

[8] B. Englot and F. S. Hover, "Three-dimensional coverage planning for an underwater inspection robot," *The International Journal of Robotics Research*, vol. 32, no. 9-10, pp. 1048–1073, 2013.

[9] P. Hu, D. Peng, J. Guo, and L. Zhen, "Local feature based multi-view discriminant analysis," *Knowledge-Based Systems*, vol. 149, pp. 34–46, 2018.

[10] P. Hu, D. Peng, Y. Sang, and Y. Xiang, "Multi-view linear discriminant analysis network," *IEEE Transactions on Image Processing*, vol. 28, no. 11, pp. 5352–5365, 2019.

[11] A. Chavez, D. L'Heureux, N. Prabhakar, M. Clark, W.-L. Law, and R. J. Prazhenica, "Homography-based state estimation for autonomous uav landing," in *AIAA Information Systems-AIAA Infotech@ Aerospace*, 2017, p. 0673.

[12] R. Spica and P. Robuffo Giordano, "A framework for active estimation: Application to structure from motion," in *52nd IEEE Conference on Decision and Control*, Dec 2013, pp. 7647–7653.

[13] R. Spica, P. R. Giordano, and F. Chaumette, "Active structure from motion: Application to point, sphere, and cylinder," *IEEE Transactions on Robotics*, vol. 30, no. 6, pp. 1499–1513, Dec 2014.

[14] P. R. Giordano, R. Spica, and F. Chaumette, "An active strategy for plane detection and estimation with a monocular camera," in *2014 IEEE International Conference on Robotics and Automation (ICRA)*, May 2014, pp. 4755–4761.

[15] O. Tahri, D. Boutat, and Y. Mezouar, "Brunovsky's linear form of incremental structure from motion," *IEEE Transactions on Robotics*, vol. 33, no. 6, pp. 1491–1499, Dec 2017.

[16] Y. Huang, L. Sithole, and T. Lee, "Structure from motion technique for scene detection using autonomous drone navigation," *IEEE Transactions on Systems, Man, and Cybernetics: Systems*, vol. 49, no. 12, pp. 2559–2570, 2019.

[17] S. Ullman, "The interpretation of structure from motion," *Proceedings of the Royal Society of London. Series B. Biological Sciences*, vol. 203, no. 1153, pp. 405–426, 1979.

[18] B. Liu, S. Gould, and D. Koller, "Single image depth estimation from predicted semantic labels," in *2010 IEEE Computer Society Conference on Computer Vision and Pattern Recognition*. IEEE, 2010, pp. 1253–1260.

[19] M. Goldman, T. Hassner, and S. Avidan, "Learn stereo, infer mono: Siamese networks for self-supervised, monocular, depth estimation," in *Proceedings of the IEEE/CVF Conference on Computer Vision and Pattern Recognition (CVPR) Workshops*, June 2019.

- [20] M. Poggi, F. Aleotti, F. Tosi, and S. Mattoccia, "Towards real-time unsupervised monocular depth estimation on cpu," in *2018 IEEE/RSJ International Conference on Intelligent Robots and Systems (IROS)*, 2018, pp. 5848–5854.
- [21] E. Galceran and M. Carreras, "A survey on coverage path planning for robotics," *Robotics and Autonomous systems*, vol. 61, no. 12, pp. 1258–1276, 2013.
- [22] V. An, Z. Qu, F. Crosby, R. Roberts, and V. An, "A triangulation-based coverage path planning," *IEEE Transactions on Systems, Man, and Cybernetics: Systems*, vol. 50, no. 6, pp. 2157–2169, 2020.
- [23] A. Yazici, G. Kirlik, O. Parlaktuna, and A. Sipahioglu, "A dynamic path planning approach for multirobot sensor-based coverage considering energy constraints," *IEEE Transactions on Cybernetics*, vol. 44, no. 3, pp. 305–314, March 2014.
- [24] K. Alexis, C. Papachristos, R. Siegwart, and A. Tzes, "Uniform coverage structural inspection path-planning for micro aerial vehicles," in *2015 IEEE International Symposium on Intelligent Control (ISIC)*, Sep. 2015, pp. 59–64.
- [25] B. Herisse, S. Oustry, T. Hamel, R. Mahony, and F. Russotto, "A general optical flow based terrain-following strategy for a vtol uav using multiple views," in *2010 IEEE International Conference on Robotics and Automation*, May 2010, pp. 3341–3348.
- [26] Y. Hamada, T. Tsukamoto, and S. Ishimoto, "Receding horizon guidance of a small unmanned aerial vehicle for planar reference path following," *Aerospace Science and Technology*, vol. 77, pp. 129–137, 2018.
- [27] M. Cai, Y. Wang, S. Wang, R. Wang, L. Cheng, and M. Tan, "Prediction-based seabed terrain following control for an underwater vehicle-manipulator system," *IEEE Transactions on Systems, Man, and Cybernetics: Systems (Early Access)*, pp. 1–10, 2019.
- [28] Y. Yang and G. Huang, "Observability analysis of aided ins with heterogeneous features of points, lines, and planes," *IEEE Transactions on Robotics*, vol. 35, no. 6, pp. 1399–1418, 2019.
- [29] F. Chaumette and S. Hutchinson, "Visual servo control. ii. advanced approaches [tutorial]," *IEEE Robotics & Automation Magazine*, vol. 14, no. 1, pp. 109–118, 2007.
- [30] J. Civera, A. J. Davison, and J. M. Montiel, "Inverse depth parametrization for monocular slam," *IEEE transactions on robotics*, vol. 24, no. 5, pp. 932–945, 2008.
- [31] R. Hartley and A. Zisserman, *Multiple view geometry in computer vision*. Cambridge university press, 2003.
- [32] H. Yserentant, "A short theory of the rayleigh–ritz method," *Computational Methods in Applied Mathematics*, vol. 13, no. 4, pp. 495–502, 2013.
- [33] MATLAB, *9.7.0.1190202 (R2019b)*. Natick, Massachusetts: The MathWorks Inc., 2019.
- [34] P. Corke, "Matlab toolboxes: robotics and vision for students and teachers," *IEEE Robotics & Automation Magazine*, vol. 14, no. 4, pp. 16–17, 2007.
- [35] T. Qin, P. Li, and S. Shen, "Vins-mono: A robust and versatile monocular visual-inertial state estimator," *IEEE Transactions on Robotics*, vol. 34, no. 4, pp. 1004–1020, 2018.
- [36] DJI, *Onboard SDK 3.0*. Shenzhen, China: DJI Inc., 2019. [Online]. Available: <https://developer.dji.com/onboard-api-reference/index.html>